

Biotransformation of Silver Released from Nanoparticle Coated Titanium Implants Revealed in Regenerating Bone

Hua Geng^{1,2}, Gowsihan Poologasundarampillai^{1,2}, Naomi Todd³, Aine Devlin-Mullin³, Katie Moore¹, Zahra Golrokhi⁴, James B. Gilchrist², Eric Jones⁴, Richard J. Potter⁴, Chris Sutcliffe⁴, Marie O'Brien¹, David. W.L. Hukins⁵, Sarah Cartmell¹, Christopher A. Mitchell³, Peter D. Lee^{1,2}*

¹School of Materials, The University of Manchester, Oxford Road, M13 9PL, UK

²Research Complex at Harwell, OX11 0FA, Harwell, UK

³Centre for Molecular Biosciences (CMB), School of Biomedical Sciences, Ulster University, Coleraine, Northern Ireland

⁴Centre for Materials and Structures, School of Engineering, the University of Liverpool, Liverpool L69 3GH, UK

⁵Department of Mechanical Engineering, School of Engineering, University of Birmingham, Birmingham, UK

*Corresponding author: Professor Peter D. Lee peter.lee@manchester.ac.uk

KEYWORDS: Silver nanoparticle coatings; atomic layer deposition; biotransformation; bone formation; osseointegration

ABSTRACT

Antimicrobial silver nanoparticle coatings have attracted interest for reducing prosthetic joint infection. However, few studies report *in vivo* investigations of the biotransformation of silver nanoparticles within the regenerating tissue and its impact on bone formation. We present a longitudinal investigation of the osseointegration of silver nanoparticle-coated additive manufactured titanium implants in rat tibial defects. Correlative imaging at different time points, using nanoscale secondary ion mass spectrometry, transmission electron microscopy (TEM), histomorphometry and 3D X-ray micro-computed tomography, provided quantitative insight from the nano to macro scales. The quality and quantity of newly formed bone is comparable between the uncoated and silver coated implants. The newly formed bone demonstrates a trabecula morphology with bone being located at the implant surface as well as at a distance at 2 weeks. Nanoscale elemental mapping of the bone-implant interface showed that silver was present primarily in the osseous tissue and was co-localized with sulfur. TEM revealed silver sulfide nano-particles in the newly regenerated bone, presenting strong evidence that the previously *in vitro* observed biotransformation of silver to silver sulfide occurs *in vivo*.

1. INTRODUCTION

Additive manufactured (AM) open-porous titanium implants¹⁻² are increasingly used in orthopaedic applications where bone fixation and load bearing are required. These open-porous implants allow desirable early bone ingrowth³ and more rapid osseointegration⁴⁻⁵. Unfortunately, the placement of prostheses is also associated with the risk of prosthetic joint infection (PJI)⁶⁻⁷, ultimately leading to delayed healing or implant failure. It has been estimated that 2.5 % of patients with primary knee and up to 20% of revision knee replacement has been affected by PJI⁸⁻⁹. Treatment of such infection with antibiotics proves to be ineffective due to biofilm formation, with the ability of the immune system to respond also being hampered¹⁰⁻¹¹. Therefore, an antimicrobial surface aimed at preventing the bacterial colonisation and biofilm formation during surgery and in the immediate postoperative period is highly desirable.

Silver based antimicrobials are of particular interest due to their broad antimicrobial spectrum and efficacy¹²⁻¹³, allowing them to inhibit both gram-positive and gram-negative bacteria with very low silver concentrations. Nanoscale silver (nano-Ag) such as silver nanoparticles (AgNPs) is more reactive than its bulk counterparts due to the large surface area-to-volume ratio¹⁴. The interaction of AgNPs with moisture and body fluid leads to the fast release of biologically active silver ions¹⁵, binding to bacterial protein or DNA¹⁶, thereby preventing bacterial adhesion and biofilm formation. In addition, ultra-thin AgNP films have been successfully incorporated onto non-planar surfaces and complex architectures by several techniques¹⁷⁻¹⁹. Atomic layer deposition (ALD), a sequential and self limiting process, provides a number of advantages for depositing an AgNP surface layer, including texturing and biocompatibility. The sub angstrom control of silver precursor deposition, coupled with the self

saturating reaction lead to the formation of uniform sized AgNPs coated onto the additive manufactured porous titanium¹⁷. In a previous study, ALD of a silver coated Ti implants was shown to be effective in reducing major pathogenic biofilm formation *in vitro*²⁰.

The remarkable antimicrobial effects of AgNPs have led to their application in a diverse range of orthopaedic implants. However, the close contact that exists between silver coated implants and bone²¹ also raises concerns regarding the potentially harmful effect associated with the uptake of the silver ions into bone and surrounding soft tissue²². AgNPs can readily penetrate the cell membrane²³, releasing ions locally to a specific tissue²⁴ and becoming internalized²⁵⁻²⁶. Therefore, a detailed study on the impact of AgNPs is required.

Considerable effort has been expended in examining the biological effect of silver on bone using a variety of cell lines, and it has been shown that the impact of AgNPs is both size-²⁷⁻²⁸ and dose-dependent²⁹⁻³³. These *in vitro* studies provide an understanding of silver interaction with the specific cell types involved in bone healing, revealing a potential reduction in possible harmful effects by controlling the initial total amount of silver. Further, recent *in vitro* evidence suggests that the silver undergoes sulfidation to silver sulfide³⁴ through complex interactions with protein (serum) and cells³⁵. This lead to the hypothesis that the biological toxicity of silver is reduced through the biotransformation of silver into silver sulfide, a more stable and less toxic compound³⁵. However, the cellular response triggered by silver, and its sulfidation to silver sulfide *in vitro*, cannot be directly used to predict tissue level response *in vivo*. Bone healing, when augmented by implants, is characterized by complex interactions between multiple cell types and the osteoconductive properties of the material³⁶⁻³⁹, all of which could be disrupted by silver.

In the majority of prior studies, there is a lack of information dealing with the harmful effects of silver on bone regeneration, with apparent inconsistencies in the results obtained. Korani et al.⁴⁰ observed an abnormal inflammatory response in lamellar bone following the dermal exposure of silver. On the contrary, Marsich et al.⁴¹ found comparable bone healing patterns without significant difference in bone contact. These contradictory results may be explained by the differences in routes of exposure (e.g. bone contact, blood contact or inhalation) and experiment end-point, inevitably raising doubts about whether silver coating is detrimental to bone healing.

To date, only a few studies have focused on the effect of silver on bone regeneration associated with implanted materials⁴¹⁻⁴². However, none have performed investigations examining multiple time-points during incorporation of implants nor have they assessed the uptake/distribution of silver in tissue upon release from an implant. These aforementioned experiments can provide particularly useful information regarding the possible biological effect of silver on bone healing and potential target tissue following the contact of new bone and silver coated devices, respectively. For these reasons, detailed *in vivo* studies are required to fully elucidate the impact of silver on bone healing.

In the present study, the quantity and quality of bone following surgical implantation of both silver coated and uncoated titanium scaffolds were assessed using both X-ray micro-computed tomography (μ CT) and histological measurements. The impact of silver coating was assessed after 2, 6 and 12 weeks *in vivo*, to identify whether the presence of silver affects bone healing or decreases new bone generation. The distributions of released silver ($^{107}\text{Ag}^-$) in addition to $^{12}\text{C}^-$, $^{40}\text{Ca}^{16}\text{O}^-$, $^{31}\text{P}^{12}\text{C}^-$, $^{32}\text{S}^-$ within adjacent tissues were quantified using nanoscale secondary

ion mass spectrometry (NanoSIMS). Transmission electron microscopy (TEM) and selected area electron diffraction (SAED) were combined to examine the newly formed bone. Correlative imaging was used combine all of these complementary techniques to investigate the bone-implant interface and the biotransformation of the silver.

2. MATERIALS AND METHODS

2.1 Fabrication and preparation of the open-porous implants

Open-porous titanium implants were fabricated by additive manufacturing as previously described⁴³. Briefly, cylindrical shaped titanium implants of 2.5 mm diameter and 1.5 mm height, as shown in Fig. 1a, were produced using a MCP Realizer 250 Selective Laser Melting (SLM) system (MCP Tooling Technologies, Lubeck, Germany). The basic material used to fabricate implants was Grade 1 commercially pure titanium (CP-Ti) powder with a modal particle diameter of 28.5 μm (Sumitomo Corp., Tokyo, Japan)⁴³. The powder layer thickness used in the build process was 50 μm ⁴³. The open-porous implants were made with a nominal porosity of 65 % and a strut diameter of 180 μm ².

Following the SLM build process, the implants were cleaned in an ultrasonic bath (VWR, Radnor, USA) with micro-90 detergent (Decon, Sussex, UK) diluted 1:20 in distilled water to remove un-fused powder. The samples were then rinsed in distilled water and dried. Once cleaned, the samples were subject to heat treatment in an inert atmosphere at 667 Pa and 1400°C (for 3 hours). Before atomic layer deposition, the sintered implants were once again sintered and cleaned using the process described above.

2.2 Atomic layer deposition (ALD) of the AgNPs coating

Surface modification of the implant samples with an ultra-thin layer of silver was carried out using direct liquid injection atomic layer deposition (ALD) in a customized Aixtron AIX 200FE AVD reactor [20]. The ALD process used has been shown to be controlled by self-limiting surface reactions, enabling the production of highly conformal nano-textured metallic silver films on complex three-dimensional structures⁴⁴. The organometallic precursor and co-reactant used in the deposition process was (hexafluoroacetylacetonato)silver(I)(1,5-cyclooctadiene) dissolved in a 0.1 M anhydrous toluene solution (Sigma-Aldrich, Germany) and propan-1-ol (HPLC grade/Fisher, Leics, UK), respectively. Each ALD cycle consisted of a four step process, starting with a 4 s dose of the silver precursors, followed by an 8 s argon (99.999%; BOC, UK) purge, and then a 4 s propan-1-ol dose and finally another 8 s argon purge. The silver precursor solution was introduced into the reactor using direct liquid injection at a rate of 17.5 $\mu\text{l/s}$ and was volatilized at 130°C, while the propan-1-ol was delivered into the reactor from a vapor-draw bottle held at room temperature ($\sim 20^\circ\text{C}$) using a Swagelok ALD valve. Each sample was coated using 500 ALD cycles to give a nominal film thickness (if uniform rather than particulate islands) of ~ 13 nm which corresponds to a rate of 0.026 nm/cycle.

2.3 Scanning Electron Microscopy

The structure of the Ti and Ti-Ag implants was characterised by scanning electron microscopy (JEOL JSM-7001F FEG-SEM, Tokyo, Japan) in secondary electron mode, using a 10 kV accelerating voltage.

2.4 Sterilization

Before implantation, all samples were soaked in ethanol for 2 hours before sterilization with ultraviolet (UV) light in a Class II biosafety cabinet (Esco, Canada)⁴⁵.

2.5 Surgical implantation

A total of thirty-six adult male Wistar rats, 10–12 weeks old and weighting 300–400 g, were used for the *in vivo* study. The experimental protocol was approved by the institutional animal care committee at the University of Ulster and National (UK Home Office) guidelines. In brief, an anesthetic drug (2.0 ml Ketaset, 100 ml/mg) and 1.0 ml Xylapan (20 ml/mg) diluted in 5 ml phosphate buffered saline (PBS) (pH 7.4, 0.5 ml/100 g) was injected to sedate the animals. For the surgical procedures, a 2.5 mm subcritical size defect was created using a trephine bur. The circular defect penetrated well into the marrow cavity. Rats were randomly divided into two groups of eighteen rats each, implanted with titanium (Ti) or silver coated titanium implants (Ti-Ag).

After healing period of 2, 6 and 12 weeks, the animals were sacrificed and the implanted tibiae were subsequently fixed in a solution of 10% buffered formal saline for X-ray micro-computed tomography (μ CT) scanning.

2.6 *Ex-vivo* X-ray micro-computed tomography (μ CT)

2.6.1. Image acquisition

Post-implantation, all implanted tibiae (n = 36) were wrapped in Parafilm M (Bemis, US) and placed in an ABS plastic tube. The scanning was performed by using a laboratory based μ CT system (Nano-focus, Phoenix|x-ray General Electric Company, Measurement and Control, Wunstorf, Germany). In order to reduce beam hardening artefacts [37], the μ CT scanner was operated at 85 kV and 111 μ A with a 0.5 mm thick copper filter. Images were reconstructed using the Datoslx software (Phoenix|x-ray) resulting in an image matrix of 990 \times 990 \times 1000 pixels with an isotropic voxel size of 5 μ m. The reconstructed images were subsequently

Accepted for publication in ACS Applied Materials & Interfaces, 05/06/17
analyzed in Avizo software (Avizo 8.0, FEI Visualization Sciences Group, Mérignac Cedex,
France) and Matlab (Mathworks Inc., Natick, Massachusetts, USA).

2.6.2. Segmentation

The segmentation procedure comprised an image filter, a global threshold and a local thresholding method ⁴⁶. In the first pass, the reconstructed data were normalized to a pre-determined reference histogram before undergoing smoothing filters (edge preserving filter and anisotropic diffusion filter) ⁴⁷, to reduce the influence of noise and artefacts. The filtered images were first pre-segmented into a 'mask' containing bone and implant areas using an Ostu algorithm ⁴⁶. After pre-segmentation, the bone was segmented from the implant area using local thresholding ⁴⁶. The boundary between the bone and implant was smoothed using the morphological operations of erosion (by one pixel) and dilation (by one pixel).

2.6.3. Quantification of the titanium scaffold and newly formed bone

After segmentation, the bone and titanium phases from each individual sample were registered with a high resolution tibia shape model and a cylindrical mask (2.5 mm in diameter and 1.5 mm in height), respectively. The overlapping of the shape model and cylindrical mask were used to generate the region of interest (ROI) in a reproducible fashion (Fig.2a). Micro-architectural parameters (1) bone ingrowth (BI) $[(\text{bone area}/\text{ROI}) \times 100\%]$, (2) bone contact (BC) $[(\text{bone contact area}/(\text{total scaffold area}) \times 100\%]$, (3) specific surface area (SSA) $[(\text{bone area}/\text{bone volume}) \times 100\%]$, (4) bone trabecular thickness (Tb.Th), and (5) trabecular separation (Tb.Sp) ⁴⁸ of the newly formed bone were analysed within the defined ROI. Strut thickness and porosity of the titanium scaffolds were measured ^{2,49}.

2.7 Histology and histomorphometry

Histological preparation of rat tibiae containing titanium implants has been previously described in detail⁵⁰. Briefly, eighteen tibial specimens containing the implants (n = 3 at 2, 6 and 12 weeks in the Ti and Ti-Ag groups) were decalcified, dehydrated, infiltrated and embedded in LR white resin (TAAB Laboratories Equipment Ltd, Berks, UK). The polymerized blocks were trimmed of excess resin and glued onto plastic microscope slides (EXAKT, *Oklahoma City*, USA). An EXAKT Vacuum Adhesive Press was used to mount the samples for UV treatment (5 minutes). Subsequently, one half of the samples were cut approximately from the centre of the Ti implant using an EXAKT 310 Macro Band System with a diamond blade (EXAKT, *Oklahoma City*, USA). The blocks were ground successively with K800, K2500, and K4000 grinding paper (EXAKT) using an EXAKT 400CS grinding system to yield ~50 -100 μm thick sections. Finally, the sections were stained with Gill's Haematoxylin III (Fisher Scientific, Loughborough, UK) and multiple staining solution before examination on a Zeiss Axiophot microscope (Zeiss; Wetzlar, Germany). Histomorphometric analysis of new bone consisted of a quantitative assessment of the bone ingrowth (BI).

2.8 Sample preparation for spectroscopic analyses

Four non-decalcified samples of tibia with implant (n = 1 at 2 weeks in the Ti group; n = 1 at 2, 6 and 12 weeks in the Ti-Ag group) were washed in distilled water and kept in a -80°C freezer (New Brunswick Scientific, Enfield, USA) for 48 h. The frozen samples were then freeze dried in a CoolSafe 100-4 freeze-drier (Scanvac-Coolsafe, Lyngby, UK) for 48 hours. At the end of the drying cycle, bone-implant samples were mounted in LR White resin (Sigma-Aldrich, Dorset, UK) and polished to a mirror finish using 1 micron diamond suspension paste (Struers,

Accepted for publication in ACS Applied Materials & Interfaces, 05/06/17
Glasgow, UK). Immediately before NanoSIMS analysis the embedded samples were coated with 10 nm of platinum.

2.9 NanoSIMS

NanoSIMS images of the bone implant samples were acquired using a CAMECA NanoSIMS 50L instrument (Cameca, Gennevilliers Cedex, France). A 16 keV Cs⁺ primary ion beam with a current of 1.8 – 2.6 pA was scanned over the surface to generate negative secondary ions. The instrument was calibrated, using standards of high concentration, to detect ¹²C⁻, ³²S⁻, ³¹P¹²C⁻, ⁴⁰Ca¹⁶O⁻, ⁴⁸Ti¹⁶O⁻ and ¹⁰⁷Ag⁻. In order to ensure that each imaged area was at steady state and to remove the platinum coating, Cs⁺ ions were implanted into the surface to achieve a dose of 1 x 10¹⁷ ions cm⁻². Six to eight regions of interest were imaged from each sample with an area of 50 × 50 μm² (512 × 512 pixels). A dwell time of 5000 μs/pixel was used with an aperture size of 300 μm (D1 = 2). Image processing was carried out using ImageJ software (U.S. National Institutes of Health, Bethesda, Maryland, USA) with OpenMIMS plugin (National Resource for Imaging Mass Spectrometry, Cambridge, Massachusetts, USA).

2.10 Sample preparation for correlative imaging

After the NanoSIMS experiments, the surface that was analyzed with NanoSIMS was polished using a 6 μm diamond suspension (Struers, Glasgow, UK) and glued onto a glass slide (Thermo Scientific, Hudson, USA). The other side of sample was further ground using K1200 and P4000 grinding paper (Struers, Glasgow, UK) until the sample was 70-90 μm thick. These sections were stained with Goldners Trichrome (method adapted from ⁵¹). Briefly, the sections were rinsed with distilled water for 15 mins and the nuclei stained for 20 mins using Weigert's Haematoxylin (Sigma-Aldrich, Dorset, UK). The sections were then rinsed with distilled water

Accepted for publication in ACS Applied Materials & Interfaces, 05/06/17
and stained with 0.01% Azophloxine for 15 mins. Sections were then rinsed with 1% acetic acid followed by staining with 2% Orange G for 3 mins and rinsed again with 1% acetic acid. Lastly, they were stained with 0.2% Light Green for 5 mins followed again by rinsing with 1% acetic acid for 5 mins. The sections were then blotted dry and imaged using Olympus SZX16 stereoscopic microscope at a range of magnifications. The histological appearance of tissues in the images is consistent, with mineralized bone staining green/dark green and fibrous tissue as orange/orange red.

2.11 TEM imaging

The Goldners Trichrome stained histological sections were polished to $\sim 30\ \mu\text{m}$ using P4000 grinding paper (Struers, Glasgow, UK). The section was then mounted in a 3.05 mm Cu folding grid with a 1 mm circular hole in the center (Agar Scientific, UK). To thin the section to electron transparency a Fischione 1050 Ar^+ mill was used. Thinning was performed at successively lower beam energies and shallower angles (with respect to the section plane). Initial beam conditions were 10 kV and $\pm 10^\circ$. Final thinning conditions were 4 kV and $\pm 6^\circ$.

To differentiate the bone and fibrous tissue, the ion beam milled bone implant sample was imaged using a stereoscopic microscope (Olympus SZX16) at a range of magnifications. The sample was then imaged using a JEOL 2100 TEM operated at 200 kV. Images and diffraction patterns were acquired up to $\sim 5\ \mu\text{m}$ from the implant surface. For imaging, a 1 s camera exposure time was used. For diffraction patterns a $\sim 0.4\ \mu\text{m}$ SA aperture and a 5 s camera exposure time were used.

2.12 Statistical Analyses

The results from μ CT (n = 6) and histomorphometry analysis (n = 3) are presented as mean \pm standard deviation. Statistical comparisons were performed with a Mann–Whitney U test. All statistical analysis was carried out using XLSTAT (Addinsoft, Inc., USA), with statistical significance considered when $p < 0.05(*)$.

3. RESULTS

3.1 Characterization of the open-porous titanium implants

The Ti implants (Fig.1a) were found to have a porosity of $67 \pm 5\%$ and the modal strut diameter was $170 \pm 20 \mu\text{m}$. This compares favorably with the original design, which aimed to have 65% porosity and $180 \mu\text{m}$ struts². The selective laser melting (SLM) of the pure Ti powders gives rise to scaffolds (Fig. 1b) with a rough surface, irregular shape and a large surface area. During the ALD deposition process, metallic AgNPs (Fig. 1c) are uniformly deposited on the porous Ti surface. From the size distribution histogram (Fig. 1d), an average particle size of $49 \pm 3 \text{ nm}$ could be estimated.

3.2 Analysis of quantity of bone using *Ex vivo* x-ray micro-computed tomography

3.2.1. Bone Ingrowth (BI)

Three-dimensional μ CT analysis of the entire implant was performed on 2, 6, and 12 week samples of rat tibia containing titanium scaffolds to assess bone ingrowth in a pre-defined ROI (Fig. 2a). Representative μ CT images (Fig. 2b-2g) qualitatively confirm bone formation progresses over time for both the uncoated and silver coated titanium scaffolds. New bone was observed at the edge and interior of the defect site at two weeks after implantation, with $35 \pm 10\%$ and $31 \pm 5\%$ of void space being replaced by irregular immature bone (Fig. 2b, 2c). At six weeks post-implantation, a higher proportion of new bone was detected along the porous

titanium implant from the surface to the center (Fig. 2d, 2e). After twelve weeks, the implant pores were almost completely filled by newly formed bone (Fig. 2f, 2g). The results of the quantitative data measured from μ CT are summarized in Table 1 and Fig. 2h. No difference in bone ingrowth was observed between the Ti and Ti-Ag groups. There were significant statistical differences in bone ingrowth between 2 and 6 weeks, and 2 and 12 weeks post-implantation ($p=0.002, 0.001$).

3.2.2. Bone Contact (BC)

The contact area in the Ti (green) and Ti-Ag (red) groups were shown in 3D (Fig. 3a-3f). An increase in bone contact length was observed as the healing period increased (from 2 – 12 weeks post-implantation) in both groups. The BC of the Ti ($56 \pm 10\%$) and the Ti-Ag group ($44 \pm 13\%$) at 6 weeks' post-implantation was significantly higher than at 2 weeks post-implantation ($20 \pm 6\%$ and $14 \pm 5\%$) ($p < 0.05$). After 12 weeks implantation, up to 82% of the implant surface was colonized by newly formed bone. Significant differences in BC were not observed between the titanium and silver coated groups. The quantitative measurements of the BC for both groups are summarized in Table 1 and Fig. 3g.

Table 1: Bone ingrowth (BI) and bone contact (BC) measured from μ CT and histology

Time (weeks)	Ti			Ti-Ag		
	μ CT		histology	μ CT		histology
	BI (%)	BC (%)	BI (%)	BI (%)	BC (%)	BI (%)
2	35 \pm 10	20 \pm 6	31 \pm 9	31 \pm 5	14 \pm 5	29 \pm 8
6	66 \pm 6	56 \pm 10	42 \pm 7	58 \pm 7	44 \pm 13	59 \pm 15
12	76 \pm 7	71 \pm 11	77 \pm 6	74 \pm 6	73 \pm 9	66 \pm 10

3.2.3. Bone Morphometric parameters

We observed an increase in trabecular thickness (Tb.Th) and a decrease in specific surface area (SSA) and trabecular separation (Tb.Sep) as the healing period increased in both groups (Fig. 4). The thickness of the newly formed bone was different between 2 and 6 weeks, and 2 and 12 weeks ($p < 0.05$). No significant differences in SSA, Tb.Th and Tb.Sep were found between the uncoated and silver coated titanium groups. There was a significant difference in SSA between 2 and 6 weeks, and 2 and 12 weeks ($p < 0.05$). In the titanium implant, there were significant differences between 2 and 6 weeks ($62 \pm 8 \mu\text{m}$ and $102 \pm 17 \mu\text{m}$, $p < 0.05$), 2 and 12 weeks ($62 \pm 8 \mu\text{m}$ and $122 \pm 28 \mu\text{m}$, $p < 0.05$) for Tb.Th. In the silver coated titanium implant, the difference in Tb.Th was only observed between 2 ($62 \pm 24 \mu\text{m}$) and 12 weeks ($129 \pm 25 \mu\text{m}$).

Table 2 Bone morphometric parameters measured from X-ray μCT ; specific surface area (SSA); trabecular thickness (Tb.Th); trabecular separation (Tb.Sep)

Time (weeks)	Ti			Ti-Ag		
	SSA	Tb.Th	Tb.Sep	SSA	Tb.Th	Tb.Sep
	($\mu\text{m}^{-1}\%$)	(μm)	(μm)	($\mu\text{m}^{-1}\%$)	(μm)	(μm)
2	65 \pm 6	62 \pm 8	139 \pm 21	58 \pm 7	62 \pm 24	163 \pm 37
6	23 \pm 2	102 \pm 17	109 \pm 20	29 \pm 2	92 \pm 9	121 \pm 44
12	21 \pm 3	122 \pm 28	108 \pm 16	19 \pm 3	129 \pm 25	120 \pm 30

3.3 Quality of newly formed bone using histology and histomorphometry

In the 2 week samples from the Ti and Ti-Ag groups newly formed bone is seen on both the periphery of the defect as well as the surface of implant, where trabecula tended to be smaller

in diameter and composed of woven bone (Fig. 5a, 5b). At 6 weeks' post-implantation, lamellar bone is more conspicuous (Fig. 5c, 5d). By 12 weeks, the gap between the implant and defect further decreased and lamellar bone predominated (Fig. 5e, 5f).

The histomorphometrical assessment of BI in the Ti and Ti-Ag group is summarized in Fig. 5g and Table 1. In both group, BI was increased significantly between 2 and 12 weeks post implantation.

3.4 Elemental mapping of newly formed bone using NanoSIMS

NanoSIMS analysis of the samples revealed local element distributions at the bone-implant interface at 2 weeks post-implantation in both the Ti (Fig. 6a-6e) and Ti-Ag groups (Fig. 6f-6j). Brighter regions of the images indicate higher counts for that elemental signal. Strong $^{40}\text{Ca}^{16}\text{O}^-$, $^{31}\text{P}^{12}\text{C}^-$ and $^{32}\text{S}^-$ signals were observed in the bone tissue, $^{48}\text{Ti}^{16}\text{O}^-$ signals were highest from the titanium implant and ^{12}C was observed in certain areas at the bone-implant interface and presumably originates from organic fragments in the bone as well as the resin.

The heterogeneous distribution of $^{40}\text{Ca}^{16}\text{O}^-$ and $^{31}\text{P}^{12}\text{C}^-$ (Fig. 6c, 6d; 6h, 6i) observed at 2 weeks' post-implantation over the trabecular network, represents a different degree of maturity of the newly formed bone. Bone growth in direct contact along the entire surface of the implant (contact osteogenesis) was observed in both groups, revealing osseointegration at early time points (Fig. 6c, 6h).

The NanoSIMS elemental maps of $^{48}\text{Ti}^{16}\text{O}^-$, $^{40}\text{Ca}^{16}\text{O}^-$, $^{32}\text{S}^-$ and $^{107}\text{Ag}^-$ signals are given in Fig. 7. The maps demonstrate the distribution of Ti (Fig. 7 i), Ca (Fig. 7 ii), S (Fig. 7 iii), Ag (Fig. 7iv), while the merged images (Fig. 7 v) of Ti, Ca and Ag at the implant interface for 2 week Ti and 2, 6 and 12 weeks Ti-Ag show the interactions. As before, Ca and S intensities are highest at

the bone tissue. Silver was detected in the Ti-Ag samples at all time points (Fig. 7b-d iv). The merged images (Fig. 7 v) reveal that silver is slowly released from the implant surface, as expected, but interestingly some becomes confined within the newly formed osseous tissue. Furthermore, co-localization of silver and sulfur was observed, where, the silver signal indicated by red arrows in Fig. 7b-d iv was highest in regions with the high intensity sulfur signal (yellow arrows in Fig. 7b-d iii). Additionally, 2 weeks post-implantation, silver in the osseous tissue was observed both at the surface of the implant as well as in the trabecula away from the implant. But at 6 and 12 weeks silver was found only at the bone attached to the surface of the implant (yellow arrow head in Fig. 7d iii, red arrow head in Fig. 7d iv).

3.5 Correlative imaging using μ CT, histology and NanoSIMS

Correlative multimodal imaging was used to quantify bone tissue within the whole defect site, to identify different tissues present in the bone-tissue interface and to visualise their elemental makeup.

At 2 weeks post-implantation, the trabecula structure of the newly formed bone is clearly observed in μ CT image (Fig. 8a). The histology image (Fig. 8b) shows both the woven bone (green/dark green) and fibrous tissue (orange). The inset of histology (Fig. 8b) shows a high magnification image of a $50 \mu\text{m}^2$ region and the corresponding NanoSIMS images of this region are shown in Fig. 8c-8g, revealing the Ti, Ca, S and Ag maps within the implant and the newly formed tissue. Calcium and sulfur are observed in the newly formed bone, co-localized with silver content ($^{107}\text{Ag}^-$) both near and distance from the implants.

At 12 weeks post-implantation, the void space around the porous implant is filled by newly formed bone, with significantly increased thickness revealed by the μ CT image (Fig. 8h).

A region of less attenuating tissue was observed at the bone-implant interface (white arrow head), which when correlated to the magnified histology image (Fig. 8i) reveals the fibrous tissue is still present at the interface. The co localisation of silver and sulfur in NanoSIMS images is only observed at the region near the bone-implant interface (Fig. 8c-8g).

3.6 TEM and SAED

TEM images and SAED patterns were collected from the bone implant interface region. Fig. 9a shows a low magnification image of a region of silver coated titanium scaffold with tissue attached to the surface of the implant. Dotted purple line delineates the interface between titanium implant and tissue. Inset of Fig. 9a shows histological image of an electron transparent tissue region near the silver coated implants. Both bone (green) and fibrous (orange) tissues were identified in close proximity to each other adjacent to the implant surface. TEM micrographs from the bone region (white box, inset in Fig. 9a) shows the distinctive ~10 nm width fibrillar structures (yellow arrows, Fig. 9b&c) with particles (red arrows, Fig. 9b&c) within these areas. Electron diffraction pattern (Fig. 9d) from the area bounded by the circle reveals the crystalline nature of the sample.

4. DISCUSSION

Prosthetic joint infection (PJI) remains a serious complication after orthopaedic surgery, which has led to a number of approaches being developed to modify bacterial adhesion and growth on the surfaces of implanted devices. AgNPs are effective in preventing bacterial adhesion, biofilm formation and subsequent PJI^{14,16,20}. An investigation by Liu et al. [63] into *in vitro* dissolution of AgNPS in biological medium showed a fast silver release profile up to 12 hours of incubation, this is the most critical period for the development of PJI (from the time of

surgery). However, AgNPs are also known to be cytotoxic *in vitro*^{27,29,31,33} and at high concentrations have neurotoxic effects *in vivo*⁵². A previous study²⁰ on AgNPs coated titanium implants showed reduced bacterial (*Staphylococcus epidermidis*) recovery and biofilm formation *in vitro*. It also showed qualitatively, *in vivo* bone formation and neovascularisation within the pores of the implants. Although several studies have reported the use of silver coated devices for orthopaedic applications, the uptake/distribution of silver in tissue upon release from an implant, and its impact on new bone formation is poorly studied. As nano scale silver is readily ionized and bioavailable, there is a need to understand the uptake by local osteogenic cells and potentially harmful effects of silver on bone formation. The present study quantifies the impact of AgNPs coating on bone formation, in addition to determining the nanoscale distribution of silver within tissues adjacent to the AM implant.

AgNPs, via the tissue fluid mediated release of metallic silver particles or Ag⁺ ions^{23,29}, are known to be involved in the generation of reactive oxygen species³¹, apoptosis²⁸ as well as replacing ions that are essential for cellular function (e.g. Ca²⁺, Mg²⁺)³³. In the present study, we describe a selective laser melted porous Ti scaffold on which a uniform and metallic nanoparticulate Ag coating was deposited by atomic layer deposition (ALD)¹⁷. Ultrastructural examination of the coating revealed discrete and narrow size distributions (49 ± 3 nm) with no discernible particle aggregation (Fig. 1c & d). Growth of ultra-thin Ag films (nominal thickness 13 nm, if it were uniform rather than particulate islands) allows near atomic scale control over the particle size as well as the total amount of silver in the coating. The impact of AgNPs on biological behavior is both size^{27,53} and dose-dependent²⁹⁻³¹; these results coupled with the complex 3D geometries required for a range of orthopaedic implants, necessitates an exacting atomic scale control of the silver deposition that can be readily achieved with the ALD process.

Here, we show by multi-modal correlative imaging techniques and quantitative histological studies that at the 2 week time-point an equivalent extent of bone ingrowth into the implanted Ti and Ti-Ag scaffolds. Specifically, after 2 weeks, bone ingrowth was observed both within the surface of the scaffold as well as the marrow cavity (MC) (Fig. 2a & b). Normal bone healing is largely mediated by osteogenic cells (principally osteoblasts and osteoclasts) in addition to mesenchymal stem cells provided by the adjacent periosteum and marrow cavity⁵⁴. In the 6 and 12 week samples, less newly formed bone was detected within the marrow cavity (Fig. 2c-5f), most-likely mediated by osteoclastic resorption on the inner surface of the regenerated cortical bone⁵⁵.

μ CT and histology measurements reveal a time-dependent increase in bone formation without/with silver coating, which is associated with a significant decrease in SSA and marked thickening of trabeculae between the 2 and 6 week samples (Fig. 2b & c; Fig. 4a). Trabecular thickening and areas of contiguous ingrowth within either Ti or Ti-Ag scaffolds is conspicuous and 2D μ CT images reveal pixel intensities that are consistent with adjacent cortical bone from 12 week samples (Fig. 2f & g; 3e & f). While correlative imaging techniques employing μ CT and histology to quantify bone ingrowth in AM open-porous titanium implant⁵⁰ are useful for confirmation of tissue morphology at the micron scale, these techniques have neither the resolution nor sensitivity to investigate nanoscale osseointegration and uptake of metallic ions by regenerating bone. To address this issue, correlative multimodal imaging was further augmented using NanoSIMS and TEM to investigate elemental mapping of the bone-implant interface across multiple length scales. Medium resolution ($\sim 10 \mu\text{m}$) μ CT imaging allowed non-

destructive 3D quantification quantity of regenerated bone within the porous implants. The higher resolution ($\sim 3 \mu\text{m}$) of histological images permits reliable distinguishing of host and regenerated bone, in addition to other types of connective tissue. The high lateral spatial resolution ($\sim 195 \text{ nm}$) afforded by NanoSIMS allowed mapping with high elemental sensitivity, and resolution of thin trabecular bone ($\sim 1 \text{ micron}$ thick) in the vicinity of implants (Fig. 6a, 7b, 8g).

Bone growth occurs within the pores of the scaffold via thin trabeculae (Fig. 2b & c) as well as directly on the surfaces of Ti and silver coated Ti implants (Fig. 6b & g). These two types of bone growth are termed distance (from defect to implant surface) and contact (from implant surface to defect) osteogenesis⁵⁶, respectively, and lead to bone formation in opposite directions and faster osseointegration as evidenced during the 2 - 12 week time points we examined (Fig. 2b–h). The extent of bone growth along titanium surfaces (measured via bone contact percentage; Fig. 3g) is not significantly different between the Ti and Ti-Ag groups, indicating that coating of Ti surfaces with AgNPs does not impact osteoconduction within open-porous titanium implants.

Eriksson et al.⁵⁷ employed Time-of-Flight SIMS (TOF-SIMS), finding that after 4 weeks of implantation in rat tibiae, hydroxyapatite fragments were present at the bone-implant interface. In our study, strong signals from $^{40}\text{Ca}^{16}\text{O}^-$ and $^{31}\text{P}^{12}\text{C}^-$ were observed at 2 weeks post-implantation, providing further confirmation of contact osteogenesis on the surface of Ti implants coated with AgNPs.

Silver nanoparticle sulfidation in osseous tissue

NanoSIMS results indicate that by 2 weeks, silver from the implant surface is released and that local dissemination results in uptake by adjacent osseous tissue (Fig. 7b iv & Fig. 8f). Macrophages, the primary phagocytic cell, arrive after 24-72 hours at the site of bone injury and are capable of rapidly solubilizing metallic silver extracellularly and then accumulating silver-sulfur nanocrystals within minutes in lysosome-like structures *in vitro*³³. A similar process has been observed following ingestion of silver coated nanowires by human type 1 alveolar epithelial cells suggesting that complexing of silver-sulfur as a possible detoxification mechanism for short-term accumulation of free Ag⁺³⁴. A recent study demonstrated that the formation of silver sulfide nanocrystals, mediated through strongly adsorbed protein coronas on silver nanoparticles, leads to reduced toxicity³⁵. Since the silver we detected in this study was associated with sulfur, it is likely that a similar pathway of detoxification occurs in regenerated bone tissue adjacent to the implant surface. This mechanism is consistent with our data showing co-localization of silver with sulfur (Fig. 7b v) and our TEM and SAED results showing its biotransformation to silver sulfide nanoparticles (Fig. 9b&9c and SAED Fig. 9d) over large sections of bone tissue. The combined NanoSIMS and TEM/SAED results provide strong evidence of the mechanism by which AgNPs detoxification occurs within regenerating bone. The association of silver sulfide only within the osseous tissue could be explained by the abundance of sulfur containing proteins (i.e. albumin)⁵⁸ and/or sulfur compounds (i.e. H₂S) generated during tissue formation^{34, 59-61}.

Since silver sulfide is less soluble than silver ions, the effective antimicrobial activity of the silver-coated implants will be influenced by the biotransformation process. However, further study is required to investigate the efficacy, mode and mechanism of antimicrobial action.

The measured SAED pattern (Fig. 9d, dashed red lines) closely matches the theoretical nano-crystalline Ag_2S pattern⁶⁴. However, some elemental silver was also indexed, and unindexed lines suggest the presence of other crystalline species such as hydroxy apatite. In addition to this, artefacts introduced during sample preparation (e.g. material sputtered from other regions) will also complicate the analysis. Distinctive ~10 nm width fibrillar structures (yellow arrowheads, Fig. 9b&c) are also visible, which we hypothesize to be collagen type I, as it is observed in the newly regenerated bone.

In vitro, the uptake of silver is considered harmful due to the internalized AgNPs being released as silver ions⁶⁵, which could generate reactive oxygen species (ROS) and cause cell death²⁹. Of significance, is that AgNPs are actively endocytosed by numerous human cell types such as mesenchymal stem cells (MSC)³¹, alveolar epithelial type I cells³⁴, HaCaT keratinocytes²⁵ and peripheral blood mononuclear cells (PBMC)²⁶ consistent with the hypothesis that the endolysosomal compartment is the route for detoxification of silver *in vitro*. Additionally, it is well described that the effects of AgNPs are dependent on both their size and cell type being investigated *in vitro*: for example, low concentrations of smaller size particles (around 50nm) (similar to the particle size observed on the surface of our ALD coated Ti-implants) are relatively benign in L929 fibroblasts²⁸, hMSC^{26,31}, human PBMC²⁶ and HaCaT keratinocytes²⁵. However, at high concentrations, small size AgNPs are toxic as demonstrated in 2 human osteosarcoma cell lines³⁰, mouse primary osteoblast and osteoclasts²⁷ and hMSC²⁹.

In vivo studies examining administration via various routes (inhalation, intravenous and intraperitoneal) have also highlighted the importance of dose and AgNP size to their toxicity. Inhalation of lower doses of AgNPs results in no measureable genotoxicity in bone marrow⁶⁶.

High doses of orally administered AgNPs result in accumulation in the kidneys as well as liver damage ⁶⁷, in addition to quantifiable bone marrow cell genotoxicity ⁶⁸. Similarly, intravenous or intraperitoneal delivery of a high dose of AgNP's results in an increased frequency of polychromatic erythrocytes in bone marrow ⁶⁹, functional suppression of the immune system ⁷⁰ or a combined hepatotoxicity and genotoxicity ⁷¹. When AgNP's are dispersed within DL-lactic-co-glycolic acid ⁷², incorporated into nanotubes ⁷³⁻⁷⁴ or immobilized on Ti ⁷⁵ prior to implantation into bone, the scaffolds are osteoconductive, well integrated show antimicrobial activity and no evidence of toxicity. Similar to these aforementioned studies, the AgNP particle size we used in our *in vivo* analysis was both small (~43 nm average) and restricted to the area of regenerating bone adjacent to the implant, resulting in excellent osseointegration with no signs of toxicity.

5. CONCLUSIONS

Our *in vivo* experiments enabled the assessment of bone tissue regeneration within a uninfected rat tibia defect in response to an antimicrobial silver nanoparticle surface coating. The silver nanoparticle-coated porous titanium implants showed comparable bone formation and osseointegration to that of the uncoated implants following 2 - 12 weeks of implantation. Correlative imaging with nanoSIMS, histomorphometry and 3D X-ray micro-computed tomography, was used to analyze silver content in tibiae implanted with these scaffolds. The results demonstrated that silver accumulation primarily occurs within the osseous tissue immediately adjacent to the surface and was co-localized to sulfur. Transmission electron microscopy and selected area electron diffraction patterns reveal the sulfidation of silver, forming less toxic Ag₂S nanoparticles within the newly formed bone.

ACKNOWLEDGEMENTS

Accepted for publication in ACS Applied Materials & Interfaces, 05/06/17

This work was made possible by the facilities and support provided by the University of Manchester and Research Complex at Harwell (RCaH), funded in part by the EPSRC (EP/I02249X/1). The AgNP ALD work was partly funded by EPSRC through the Liverpool Knowledge Transfer Account (EP/H500146/1). We are also grateful for the support and helpful comments provided our colleagues Dr. Kamel Madi, Dr. Yiqiang Wang, Dr. Amy Nommeots-Nomm and Dr. Robert Atwood, together with Dr. Shilei Zhang (Oxford). Data Statement: Representative data from the experiments is presented in the graphs in this manuscript; the underlying data is not provided online due to its huge size.

REFERENCE

1. Amin Yavari, S.; Loozen, L.; Paganelli, F. L.; Bakhshandeh, S.; Lietaert, K.; Groot, J. A.; Fluit, A. C.; Boel, C. E.; Alblas, J.; Vogely, H. C., Antibacterial Behavior of Additively Manufactured Porous Titanium with Nanotubular Surfaces Releasing Silver Ions. *ACS applied materials & interfaces* **2016**, *8*, 17080-17089.
2. Kim, T. B.; Yue, S.; Zhang, Z.; Jones, E.; Jones, J. R.; Lee, P. D., Additive Manufactured Porous Titanium Structures: Through-Process Quantification of Pore and Strut Networks. *J. Mater. Process. Technol.* **2014**, *214*, 2706-2715.
3. Braem, A.; Chaudhari, A.; Cardoso, M. V.; Schrooten, J.; Duyck, J.; Vleugels, J., Peri- and Intra-Implant Bone Response to Microporous Ti Coatings with Surface Modification. *Acta Biomater.* **2014**, *10*, 986-995.
4. Xiu, P.; Jia, Z.; Lv, J.; Yin, C.; Cheng, Y.; Zhang, K.; Song, C.; Leng, H.; Zheng, Y.; Cai, H., Tailored Surface Treatment of 3d Printed Porous Ti6Al4V by Microarc Oxidation for Enhanced Osseointegration Via Optimized Bone in-Growth Patterns and Interlocked Bone/Implant Interface. *ACS Applied Materials & Interfaces* **2016**, *8*, 17964-17975.
5. Zhang, Z.; Jones, D.; Yue, S.; Lee, P.; Jones, J.; Sutcliffe, C.; Jones, E., Hierarchical Tailoring of Strut Architecture to Control Permeability of Additive Manufactured Titanium Implants. *Materials Science and Engineering: C* **2013**, *33*, 4055-4062.
6. Arciola, C. R.; Campoccia, D.; Speziale, P.; Montanaro, L.; Costerton, J. W., Biofilm Formation in Staphylococcus Implant Infections. A Review of Molecular Mechanisms and Implications for Biofilm-Resistant Materials. *Biomaterials* **2012**, *33*, 5967-5982.
7. Zimmerli, W.; Trampuz, A.; Ochsner, P. E., Prosthetic-Joint Infections. *New Engl. J. Med.* **2004**, *351*, 1645-1654.
8. Kaltsas, D. S., Infection after Total Hip Arthroplasty. *Ann. R. Coll. Surg. Engl.* **2004**, *86*, 267.
9. Meehan, J.; Jamali, A. A.; Nguyen, H., Prophylactic Antibiotics in Hip and Knee Arthroplasty. *J. Bone Joint Surg. Am.* **2009**, *91*, 2480-2490.

10. Jennison, T.; McNally, M.; Pandit, H., Prevention of Infection in External Fixator Pin Sites. *Acta Biomater.* **2014**, *10*, 595-603.
11. Römling, U.; Balsalobre, C., Biofilm Infections, Their Resilience to Therapy and Innovative Treatment Strategies. *J. Intern. Med.* **2012**, *272*, 541-561.
12. Ramalingam, B.; Parandhaman, T.; Das, S. K., Antibacterial Effects of Biosynthesized Silver Nanoparticles on Surface Ultrastructure and Nanomechanical Properties of Gram-Negative Bacteria Viz. Escherichia Coli and Pseudomonas Aeruginosa. *ACS applied materials & interfaces* **2016**, *8*, 4963-4976.
13. Eckhardt, S.; Brunetto, P. S.; Gagnon, J.; Priebe, M.; Giese, B.; Fromm, K. M., Nanobio Silver: Its Interactions with Peptides and Bacteria, and Its Uses in Medicine. *Chem. Rev.* **2013**, *113*, 4708-4754.
14. Schacht, V.; Neumann, L.; Sandhi, S.; Chen, L.; Henning, T.; Klar, P.; Theophel, K.; Schnell, S.; Bunge, M., Effects of Silver Nanoparticles on Microbial Growth Dynamics. *J. Appl. Microbiol.* **2013**, *114*, 25-35.
15. Feng, Q.; Wu, J.; Chen, G.; Cui, F.; Kim, T.; Kim, J., A Mechanistic Study of the Antibacterial Effect of Silver Ions on Escherichia Coli and Staphylococcus Aureus. *J. Biomed. Mater. Res.* **2000**, *52*, 662-668.
16. Jung, W. K.; Koo, H. C.; Kim, K. W.; Shin, S.; Kim, S. H.; Park, Y. H., Antibacterial Activity and Mechanism of Action of the Silver Ion in Staphylococcus Aureus and Escherichia Coli. *Appl. Environ. Microbiol.* **2008**, *74*, 2171-2178.
17. Golrokhi, Z.; Chalker, S.; Sutcliffe, C. J.; Potter, R. J., Self Limiting Atomic Layer Deposition of Conformal Nano-Structured Silver Films. *Applied Surface Science* **2015**, *364*, 789-797.
18. Ewald, A.; Glückermann, S. K.; Thull, R.; Gbureck, U., Antimicrobial Titanium/Silver Pvd Coatings on Titanium. *Biomedical engineering online* **2006**, *5*, 22.
19. Zhang, W.; Luo, Y.; Wang, H.; Jiang, J.; Pu, S.; Chu, P. K., Ag and Ag/N 2 Plasma Modification of Polyethylene for the Enhancement of Antibacterial Properties and Cell Growth/Proliferation. *Acta Biomater.* **2008**, *4*, 2028-2036.
20. Devlin - Mullin, A.; Todd, N. M.; Golrokhi, Z.; Geng, H.; Konerding, M. A.; Ternan, N. G.; Hunt, J. A.; Potter, R. J.; Sutcliffe, C.; Jones, E., Atomic Layer Deposition of a Silver Nanolayer on Advanced Titanium Orthopedic Implants Inhibits Bacterial Colonization and Supports Vascularized De Novo Bone Ingrowth. *Advanced Healthcare Materials* **2017**, 10.1002/adhm.201700033.
21. Brennan, S.; Fhoghlú, C. N.; Devitt, B.; O'Mahony, F.; Brabazon, D.; Walsh, A., Silver Nanoparticles and Their Orthopaedic Applications. *Bone & Joint Journal* **2015**, *97*, 582-589.
22. Fischer, H. C.; Chan, W. C., Nanotoxicity: The Growing Need for in Vivo Study. *Curr. Opin. Biotechnol.* **2007**, *18*, 565-571.
23. McShan, D.; Ray, P. C.; Yu, H., Molecular Toxicity Mechanism of Nanosilver. *J. Food Drug Anal.* **2014**, *22*, 116-127.
24. Milić, M.; Leitinger, G.; Pavičić, I.; Zebić Avdičević, M.; Dobrović, S.; Goessler, W.; Vinković Vrček, I., Cellular Uptake and Toxicity Effects of Silver Nanoparticles in Mammalian Kidney Cells. *J. Appl. Toxicol.* **2015**, *35*, 581-592.
25. Lu, W.; Senapati, D.; Wang, S.; Tovmachenko, O.; Singh, A. K.; Yu, H.; Ray, P. C., Effect of Surface Coating on the Toxicity of Silver Nanomaterials on Human Skin Keratinocytes. *Chem. Phys. Lett.* **2010**, *487*, 92-96.

26. Pauksch, L.; Rohnke, M.; Schnettler, R.; Lips, K. S., Silver Nanoparticles Do Not Alter Human Osteoclastogenesis but Induce Cellular Uptake. *Toxicology Reports* **2014**, *1*, 900-908.
27. Albers, C. E.; Hofstetter, W.; Siebenrock, K. A.; Landmann, R.; Klenke, F. M., In Vitro Cytotoxicity of Silver Nanoparticles on Osteoblasts and Osteoclasts at Antibacterial Concentrations. *Nanotoxicology* **2013**, *7*, 30-36.
28. Park, M. V.; Neigh, A. M.; Vermeulen, J. P.; de la Fonteyne, L. J.; Verharen, H. W.; Briedé, J. J.; van Loveren, H.; de Jong, W. H., The Effect of Particle Size on the Cytotoxicity, Inflammation, Developmental Toxicity and Genotoxicity of Silver Nanoparticles. *Biomaterials* **2011**, *32*, 9810-9817.
29. Pauksch, L.; Hartmann, S.; Rohnke, M.; Szalay, G.; Alt, V.; Schnettler, R.; Lips, K. S., Biocompatibility of Silver Nanoparticles and Silver Ions in Primary Human Mesenchymal Stem Cells and Osteoblasts. *Acta Biomater.* **2014**, *10*, 439-449.
30. Harges, J.; Streitburger, A.; Ahrens, H.; Nusselt, T.; Gebert, C.; Winkelmann, W.; Battmann, A.; Gosheger, G., The Influence of Elementary Silver Versus Titanium on Osteoblasts Behaviour in Vitro Using Human Osteosarcoma Cell Lines. *Sarcoma* **2007**.
31. Sengstock, C.; Diendorf, J.; Epple, M.; Schildhauer, T. A.; Köller, M., Effect of Silver Nanoparticles on Human Mesenchymal Stem Cell Differentiation. *Beilstein journal of nanotechnology* **2014**, *5*, 2058-2069.
32. Wu, A. C.; Raggatt, L. J.; Alexander, K. A.; Pettit, A. R., Unraveling Macrophage Contributions to Bone Repair. *BoneKEy reports* **2013**, *2*.
33. Loch, L. J.; Larsen, A.; Stoltenberg, M.; Danscher, G., Cultured Macrophages Cause Dissolucytosis of Metallic Silver. *Histol. Histopathol.* **2009**, *24*, 167.
34. Chen, S.; Goode, A. E.; Sweeney, S.; Theodorou, I. G.; Thorley, A. J.; Ruenraroengsak, P.; Chang, Y.; Gow, A.; Schwander, S.; Skepper, J., Sulfidation of Silver Nanowires inside Human Alveolar Epithelial Cells: A Potential Detoxification Mechanism. *Nanoscale* **2013**, *5*, 9839-9847.
35. Miclăuş, T.; Beer, C.; Chevallier, J.; Scavenius, C.; Bochenkov, V. E.; Enghild, J. J.; Sutherland, D. S., Dynamic Protein Coronas Revealed as a Modulator of Silver Nanoparticle Sulphidation in Vitro. *Nature Communications* **2016**, *7*.
36. Albrektsson, T.; Johansson, C., Osteoinduction, Osteoconduction and Osseointegration. *Eur. Spine J.* **2001**, *10*, S96-S101.
37. Stevens, M. M., Biomaterials for Bone Tissue Engineering. *Materials today* **2008**, *11*, 18-25.
38. Webster, T. J.; Patel, A. A.; Rahaman, M.; Bal, B. S., Anti-Infective and Osteointegration Properties of Silicon Nitride, Poly (Ether Ether Ketone), and Titanium Implants. *Acta Biomater.* **2012**, *8*, 4447-4454.
39. Einhorn, T. A.; Gerstenfeld, L. C., Fracture Healing: Mechanisms and Interventions. *Nature Reviews Rheumatology* **2015**, *11*, 45-54.
40. Korani, M.; Rezayat, S. M.; Arbabi Bidgoli, S., Sub-Chronic Dermal Toxicity of Silver Nanoparticles in Guinea Pig: Special Emphasis to Heart, Bone and Kidney Toxicities. *Iranian Journal of Pharmaceutical Research* **2013**, *12*, 511-519.
41. Marsich, E.; Travan, A.; Donati, I.; Turco, G.; Kulkova, J.; Moritz, N.; Aro, H.; Crosera, M.; Paoletti, S., Biological Responses of Silver-Coated Thermosets: An in Vitro and in Vivo Study. *Acta Biomater.* **2013**, *9*, 5088-5099.

42. Qin, H.; Cao, H.; Zhao, Y.; Jin, G.; Cheng, M.; Wang, J.; Jiang, Y.; An, Z.; Zhang, X.; Liu, X., Antimicrobial and Osteogenic Properties of Silver-Ion-Implanted Stainless Steel. *ACS applied materials & interfaces* **2015**, *7*, 10785-10794.
43. Mullen, L.; Stamp, R. C.; Fox, P.; Jones, E.; Ngo, C.; Sutcliffe, C. J., Selective Laser Melting: A Unit Cell Approach for the Manufacture of Porous, Titanium, Bone in - Growth Constructs, Suitable for Orthopedic Applications. Ii. Randomized Structures. *Journal of Biomedical Materials Research Part B: Applied Biomaterials* **2010**, *92*, 178-188.
44. Chalker, P.; Romani, S.; Marshall, P.; Rosseinsky, M.; Rushworth, S.; Williams, P., Liquid Injection Atomic Layer Deposition of Silver Nanoparticles. *Nanotechnology* **2010**, *21*, 405602.
45. Della Valle, C.; Visai, L.; Santin, M.; Cigada, A.; Candiani, G.; Pezzoli, D.; Arciola, C. R.; Imbriani, M.; Chiesa, R., A Novel Antibacterial Modification Treatment of Titanium Capable to Improve Osseointegration. *Int. J. Artif. Organs* **2012**, *35*, 864-875.
46. Otsu, N., A Threshold Selection Method from Gray-Level Histograms. *IEEE Trans. on Sys. Man and Cybernetics* **1979**, *9*, 62-65.
47. Chao, S. M.; Tsai, D. M.; Chiu, W. Y.; Li, W. C. In *Anisotropic Diffusion-Based Detail-Preserving Smoothing for Image Restoration*, Image Processing (ICIP), 2010 17th IEEE International Conference on, IEEE: **2010**; pp 4145-4148.
48. Parfitt, A. M.; Drezner, M. K.; Glorieus, F. H.; Kanis, J. A.; Malluche, H.; Meunier, P. J.; Ott, S. M.; Recker, R. R., Bone Histomorphometry: Standardization of Nomenclature, Symbols, and Units. *J. Bone Miner. Res.* **1987**, *2*, 595-610.
49. Atwood, R.; Jones, J.; Lee, P.; Hensch, L., Analysis of Pore Interconnectivity in Bioactive Glass Foams Using X-Ray Microtomography. *Scripta Materialia* **2004**, *51*, 1029-1033.
50. Geng, H.; Todd, N. M.; Devlin-Mullin, A.; Poologasundarampillai, G.; Kim, T. B.; Madi, K.; Cartmell, S.; Mitchell, C. A.; Jones, J. R.; Lee, P. D., A Correlative Imaging Based Methodology for Accurate Quantitative Assessment of Bone Formation in Additive Manufactured Implants. *J. Mater. Sci. Mater. Med.* **2016**, *27*, 1-9.
51. Rentsch, C. a. S. W. a. R. S., Comprehensive Histological Evaluation of Bone Implants *Biomatter* **2014**, *4*.
52. Chandirasekar, S.; Chandrasekaran, C.; Muthukumarasamyvel, T.; Sudhandiran, G.; Rajendiran, N., Sodium Cholate-Templated Blue Light-Emitting Ag Subnanoclusters: In Vivo Toxicity and Imaging in Zebrafish Embryos. *ACS applied materials & interfaces* **2015**, *7*, 1422-1430.
53. Chen, L. Q.; Fang, L.; Ling, J.; Ding, C. Z.; Kang, B.; Huang, C. Z., Nanotoxicity of Silver Nanoparticles to Red Blood Cells: Size Dependent Adsorption, Uptake, and Hemolytic Activity. *Chem. Res. Toxicol.* **2015**, *28*, 501-509.
54. Mizuno, K.; Mineo, K.; Tachibana, T.; Sumi, M.; Matsubara, T.; Hirohata, K., The Osteogenetic Potential of Fracture Haematoma. Subperiosteal and Intramuscular Transplantation of the Haematoma. *Bone & Joint Journal* **1990**, *72*, 822-829.
55. Teitelbaum, S. L., Bone Resorption by Osteoclasts. *Science* **2000**, *289*, 1504-1508.
56. Davies, J. E., Understanding Peri-Implant Endosseous Healing. *J. Dent. Educ.* **2003**, *67*, 932-949.
57. Eriksson, C.; Malmberg, P.; Nygren, H., Time - of - Flight Secondary Ion Mass Spectrometric Analysis of the Interface between Bone and Titanium Implants. *Rapid Commun. Mass Spectrom.* **2008**, *22*, 943-949.

58. Yadav, M.; Singh, A.; Ali, S.; Rizivi, N.; Hussain, S. R.; Kumar, V., Role of Serum Albumin in Fracture Healing. *International Journal of Biomedical Research* **2015**, *6*, 452-455.
59. Lin, V. S.; Lippert, A. R.; Chang, C. J., Cell-Trappable Fluorescent Probes for Endogenous Hydrogen Sulfide Signaling and Imaging H₂O₂-Dependent H₂S Production. *Proceedings of the National Academy of Sciences* **2013**, *110*, 7131-7135.
60. Waer, S. M., The Effect of Some Metal Ions on Volatile Sulfur-Containing Compounds Originating from the Oral Cavity. *Acta Odontol. Scand.* **1997**, *55*, 261-264.
61. Drake, P. L.; Hazelwood, K. J., Exposure-Related Health Effects of Silver and Silver Compounds: A Review. *Ann. Occup. Hyg.* **2005**, *49*, 575-585.
62. Choi, O.; Clevenger, T. E.; Deng, B.; Surampalli, R. Y.; Ross, L.; Hu, Z., Role of Sulfide and Ligand Strength in Controlling Nanosilver Toxicity. *Water Res.* **2009**, *43* (7), 1879-1886.
63. Liu, J.; Sonshine, D. A.; Shervani, S.; Hurt, R. H., Controlled Release of Biologically Active Silver from Nanosilver Surfaces. *ACS nano* **2010**, *4* (11), 6903-6913.
64. FRUEH, A. J., The Crystallography of Silver Sulfide, Ag₂S. *Zeitschrift für Kristallographie-Crystalline Materials* **1958**, *110*, 136-144.
65. Hsiao, I.-L.; Hsieh, Y.-K.; Wang, C.-F.; Chen, I.-C.; Huang, Y.-J., Trojan-Horse Mechanism in the Cellular Uptake of Silver Nanoparticles Verified by Direct Intra- and Extracellular Silver Speciation Analysis. *Environ. Sci. Technol.* **2015**, *49*, 3813-3821.
66. Kim, J. S.; Sung, J. H.; Ji, J. H.; Song, K. S.; Lee, J. H.; Kang, C. S.; Yu, I. J., In Vivo Genotoxicity of Silver Nanoparticles after 90-Day Silver Nanoparticle Inhalation Exposure. *Safety and health at work* **2011**, *2*, 34-38.
67. Kim, Y. S.; Kim, J. S.; Cho, H. S.; Rha, D. S.; Kim, J. M.; Park, J. D.; Choi, B. S.; Lim, R.; Chang, H. K.; Chung, Y. H., Twenty-Eight-Day Oral Toxicity, Genotoxicity, and Gender-Related Tissue Distribution of Silver Nanoparticles in Sprague-Dawley Rats. *Inhalation Toxicol.* **2008**, *20*, 575-583.
68. Patlolla, A. K.; Hackett, D.; Tchounwou, P. B., Genotoxicity Study of Silver Nanoparticles in Bone Marrow Cells of Sprague-Dawley Rats. *Food Chem. Toxicol.* **2015**, *85*, 52-60.
69. Dobrzyńska, M. M.; Gajowik, A.; Radzikowska, J.; Lankoff, A.; Dušinská, M.; Kruszewski, M., Genotoxicity of Silver and Titanium Dioxide Nanoparticles in Bone Marrow Cells of Rats in Vivo. *Toxicology* **2014**, *315*, 86-91.
70. Vandebriel, R. J.; Tonk, E. C.; de la Fonteyne-Blankestijn, L. J.; Gremmer, E. R.; Verharen, H. W.; van der Ven, L. T.; van Loveren, H.; de Jong, W. H., Immunotoxicity of Silver Nanoparticles in an Intravenous 28-Day Repeated-Dose Toxicity Study in Rats. *Part. Fibre Toxicol.* **2014**, *11*, 1.
71. El Mahdy, M. M.; Eldin, T. A. S.; Aly, H. S.; Mohammed, F. F.; Shaalan, M. I., Evaluation of Hepatotoxic and Genotoxic Potential of Silver Nanoparticles in Albino Rats. *Exp. Toxicol. Pathol.* **2015**, *67*, 21-29.
72. Liu, Y.; Zheng, Z.; Zara, J. N.; Hsu, C.; Soofer, D. E.; Lee, K. S.; Siu, R. K.; Miller, L. S.; Zhang, X.; Carpenter, D., The Antimicrobial and Osteoinductive Properties of Silver Nanoparticle/Poly (DL-Lactic-Co-Glycolic Acid)-Coated Stainless Steel. *Biomaterials* **2012**, *33*, 8745-8756.
73. Cheng, H.; Li, Y.; Huo, K.; Gao, B.; Xiong, W., Long - Lasting in Vivo and in Vitro Antibacterial Ability of Nanostructured Titania Coating Incorporated with Silver Nanoparticles. *Journal of Biomedical Materials Research Part A* **2014**, *102*, 3488-3499.

74. Cheng, H.; Xiong, W.; Fang, Z.; Guan, H.; Wu, W.; Li, Y.; Zhang, Y.; Alvarez, M. M.; Gao, B.; Huo, K., Strontium (Sr) and Silver (Ag) Loaded Nanotubular Structures with Combined Osteoinductive and Antimicrobial Activities. *Acta Biomater.* **2015**, *31*, 388-400.

75. Zhu, Y.; Cao, H.; Qiao, S.; Wang, M.; Gu, Y.; Luo, H.; Meng, F.; Liu, X.; Lai, H., Hierarchical Micro/Nanostructured Titanium with Balanced Actions to Bacterial and Mammalian Cells for Dental Implants. *International journal of nanomedicine* **2015**, *10*, 6659.

FIGURE LEGENDS

Fig. 1. (a) Macroscopic SEM-SE image of the additively manufactured porous titanium scaffold. High-resolution SEM images of (b) titanium scaffolds and (c) silver coated titanium scaffolds. (d) Size distribution histogram of silver particles (125 °C for 500 ALD cycles).

Fig. 2. (a) X-ray micro CT (μ CT) images of bone formation within the region of interest (ROI). Bone ingrowth was quantified at (b,c) 2, (d,e) 6 and (f,g) 12 weeks post-operation. Arrows indicate the newly regenerated bone in the uncoated (green) and silver coated group (red). (h) The amount of bone ingrowth, expressed as the percentage bone volume within ROI as measured by μ CT. Statistical significance (*) was considered where $p < 0.05$. Scale bars 500 μ m.

Fig. 3. μ CT images of bone to titanium scaffold contact with and without silver coating at (a, b) 2, (c, d) 6 and (e, f) 12 weeks post-implantation. (g) Bone contact, expressed as the percentage of bone implant contact within the region of interest (ROI) as measured by μ CT. Statistical significance (*) was considered where $p < 0.05$. Scale bars 500 μ m.

Fig. 4. Bone morphometric parameters. (a) Specific surface area (SSA), (b) trabecular bone thickness (Tb.Th) and (c) trabecular bone separation (Tb.Sep) as measured by μ CT. Representative μ CT images are inset into (a). Statistical significance (*) was considered where $p < 0.05$. Scale bars 200 μ m.

Fig. 5. Representative histology images of haematoxylin and multiple stained bone-titanium implant sections at (a, b) 2, (c, d) 6 and (e, f) 12 weeks post-implantation. (g) Bone ingrowth in Ti and Ti-Ag groups ($n = 3$) is measured from histomorphometry. Statistical significant was considered where $p < 0.05$. Scale bars 200 μ m.

Fig. 6. NanoSIMS elemental images of bone-implant interface in (a-e) titanium and (f-j) silver coated titanium implants after 2 weeks implantation. The NanoSIMS images ($50 \times 50 \mu\text{m}^2$) were

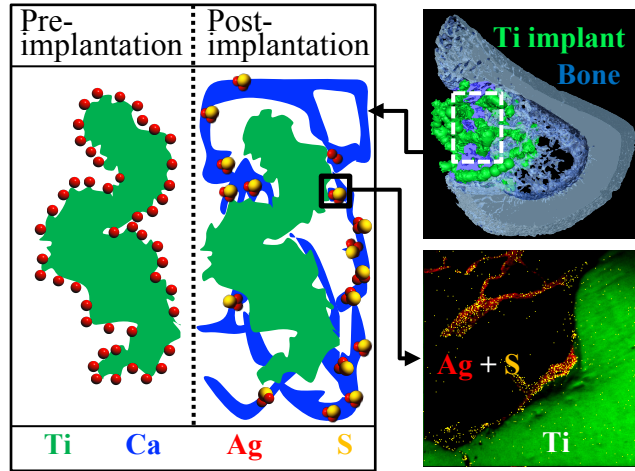
acquired using CAMECA NanoSIMS 50L instrument equipped with Cs⁺ primary ion beam. Images reveal the co-localization of sulfur (measured as ³²S⁻) and Ca/P (measured as ⁴⁰Ca¹⁶O⁻ and ³¹P¹²C⁻, respectively). The arrows highlight the direct contact between the newly formed osseous tissue (measured as ⁴⁰Ca¹⁶O⁻ and ³¹P¹²C⁻, respectively) and implants (measured as ⁴⁸Ti¹⁶O⁻) in both groups. Scale bars 10 μm.

Fig. 7. NanoSIMS elemental images of bone-implant interface after (a-b) 2, (c) 6 and (d) 12 weeks implantation. The NanoSIMS images of ⁴⁸Ti¹⁶O⁻ (i), ⁴⁰Ca¹⁶O⁻ (ii), ¹⁰⁷Ag⁻ (iii), ³²S⁻ (iv) and merged (v) (superposition of ⁴⁸Ti¹⁶O⁻, ⁴⁰Ca¹⁶O⁻ and ¹⁰⁷Ag⁻) were used to determine the uptake of silver. A comparison of images in Ti and Ti-Ag group at 2 weeks post-implantation (aii, aiv, bii, biv) reveals the silver (measured as ¹⁰⁷Ag⁻) is taken up into the osseous tissue (measured as ⁴⁰Ca¹⁶O⁻). At 2 weeks post-implantation, the NanoSIMS images of ¹⁰⁷Ag⁻ (red arrows) and ³²S⁻ (yellow arrows) reveal the co-localization of silver and sulfur in the newly formed bone. At 6 and 12 weeks post-implantation, co-localization of ¹⁰⁷Ag⁻ (red arrow head) and ³²S⁻ (yellow arrow head) is only observed at the region near the periphery of implant. Scale bars 10 μm.

Fig. 8. (a-n) Correlative imaging of μCT, Goldners trichrome stained histology and NanoSIMS show different tissue types and the uptake of silver. At 2 weeks post-implantation, the newly formed bone is observed in both (a) μCT and (b) histology image. Correlative (b) histology and (c-g) NanoSIMS images shows the woven bone and fibrous tissue at the bone-implant interface. The co-localization of silver and sulfur occurs in the newly formed woven bone. At 12 weeks post-implantation, the void space of the porous implant is filled with more matured bone, as shown in (h) μCT image. Correlative (i) histology and NanoSIMS images (j-n) show the lamellar bone and fibrous tissue at the bone-implant interface.

Fig. 9. (a) TEM image of a region containing a silver coated titanium scaffold and surrounding tissue at two weeks post implantation. The dotted line delineates the interface between titanium implant and regenerated tissue. Inset (from boxed area) is a histological image of an electron transparent tissue region adjacent to the implant that shows mineralized bone (stained green) next to fibrous connective tissue (stained orange). Higher magnification TEM images (b) & (c) from the area of bone identified in the inset reveals distinctive ~10 nm width fibrillar structures (yellow arrowheads) and electron dense particles (red arrowheads). The association of the fibrillary structures with the electron dense particles is conspicuous (c). A selected area electron diffraction (SAED) pattern of the encircled area in (b) was performed using a selected area aperture size of ~400 nm. The concentric rings (d) imply the presence of a crystalline nanoparticulate phase. The SAED pattern observed matches the standard silver sulfide pattern (dotted arc line in red) strongly supporting the hypothesis that the particles in the TEM images are silver sulfide. Scale bars = 10 μm in (a) and inset; (b) = 100 nm, (c) = 20 nm and (d) = 5 nm⁻¹ (in reciprocal space).

Graphical abstract



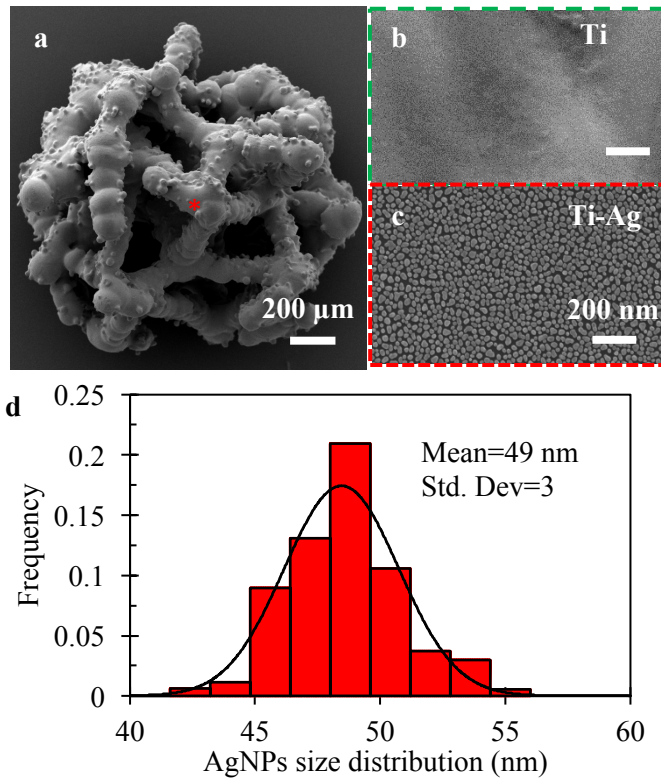


Fig. 1. (a) Macroscopic SEM-SE image of the additively manufactured porous titanium scaffold. High-resolution SEM images of (b) titanium scaffolds and (c) silver coated titanium scaffolds. (d) Size distribution histogram of silver particles (125 °C for 500 ALD cycles).

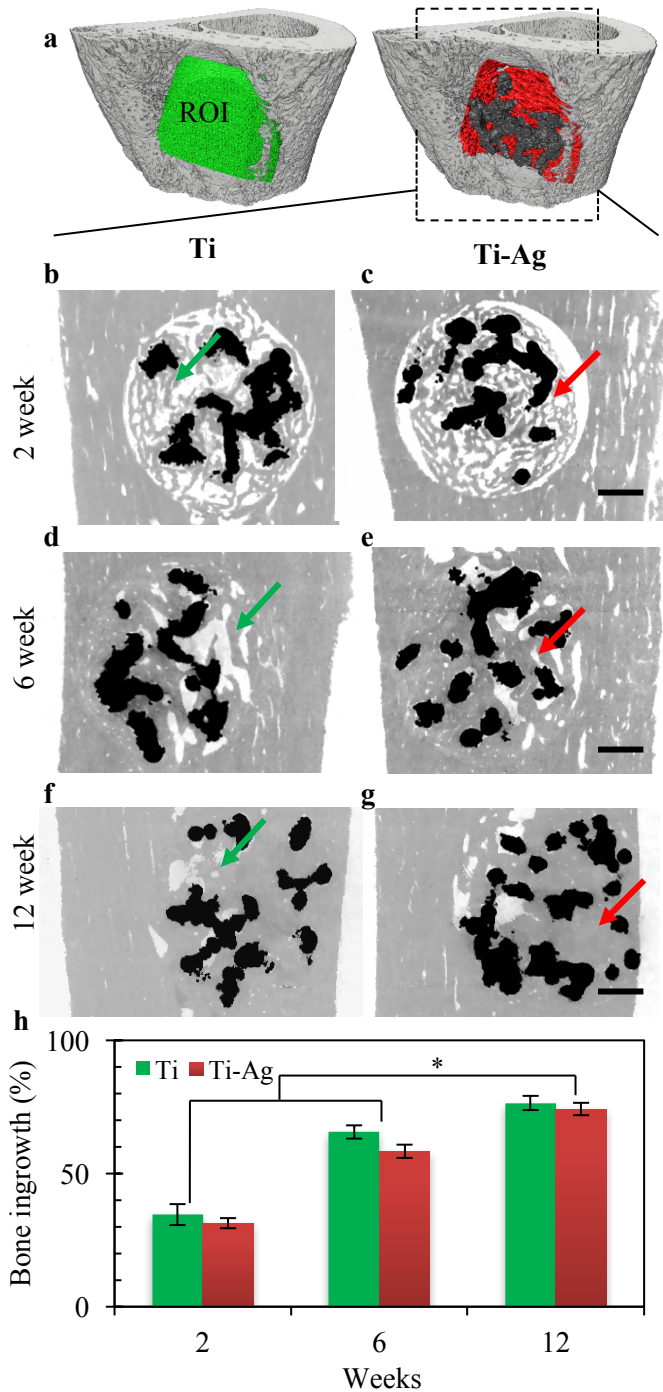


Fig. 2. (a) X-ray micro CT (μ CT) images of bone formation within the region of interest (ROI). Bone ingrowth was quantified at (b,c) 2, (d,e) 6 and (f,g) 12 weeks post-operation. Arrows indicate the newly regenerated bone in the uncoated (green) and silver coated group (red). (h) The amount of bone ingrowth, expressed as the percentage bone volume within ROI as measured by μ CT. Statistical significance (*) was considered where $p < 0.05$. Scale bars 500 μ m.

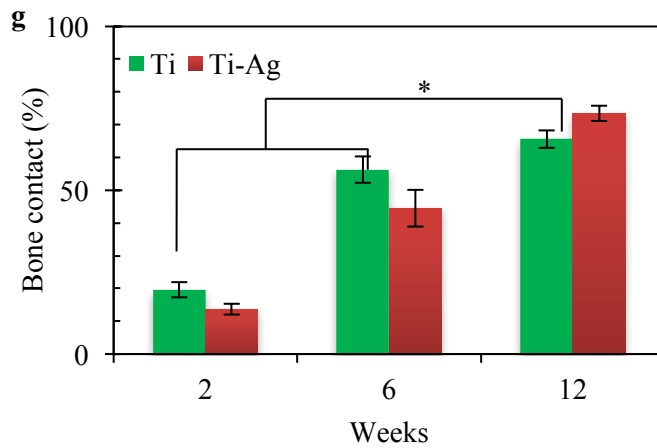
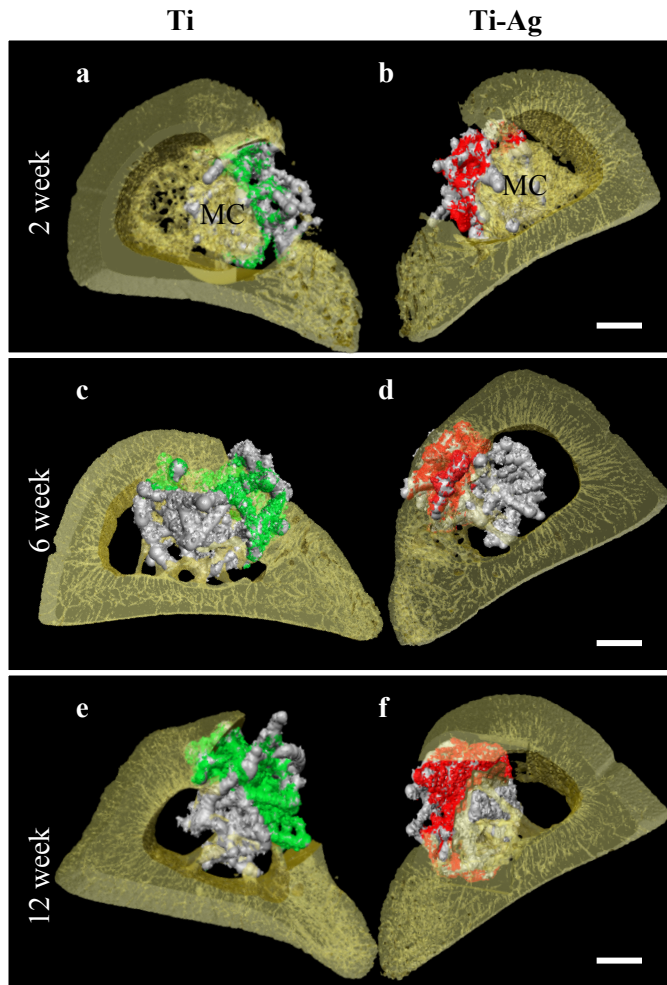


Fig. 3. μ CT images of bone to titanium scaffold contact with and without silver coating at (a, b) 2, (c, d) 6 and (e, f) 12 weeks post-implantation. (g) Bone contact, expressed as the percentage of bone implant contact within the region of interest (ROI) as measured by μ CT. Statistical significance (*) was considered where $p < 0.05$. Scale bars 500 μ m.

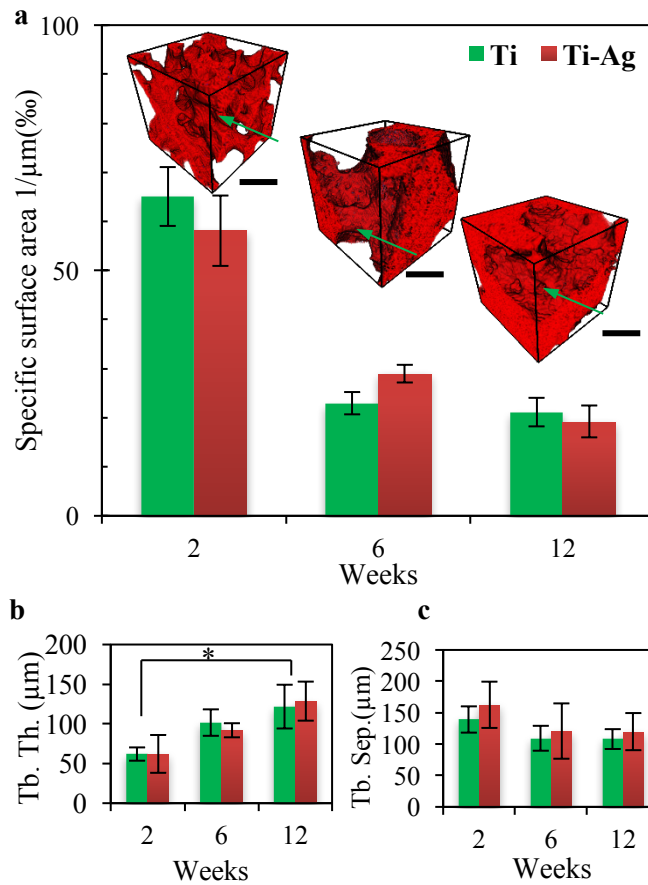


Fig. 4. Bone morphometric parameters. (a) Specific surface area (SSA), (b) trabecular bone thickness (Tb.Th) and (c) trabecular bone separation (Tb.Sep) as measured by μ CT. Representative μ CT images are inset into (a). Statistical significance (*) was considered where $p < 0.05$. Scale bars 200 μ m.

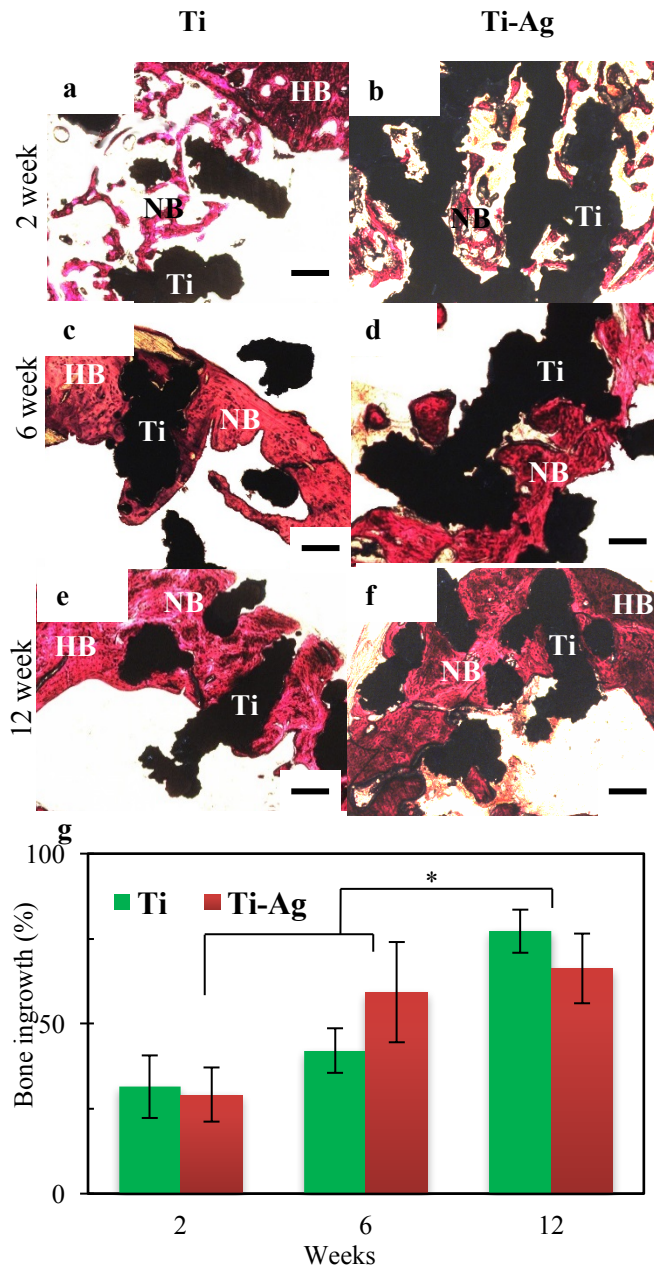


Fig. 5. Representative histology images of haematoxylin and multiple stained bone-titanium implant sections at (a, b) 2, (c, d) 6 and (e, f) 12 weeks post-implantation. (g) Bone ingrowth in Ti and Ti-Ag groups ($n = 3$) is measured from histomorphometry. Statistical significant was considered where $p < 0.05$. Scale bars 200 μm .

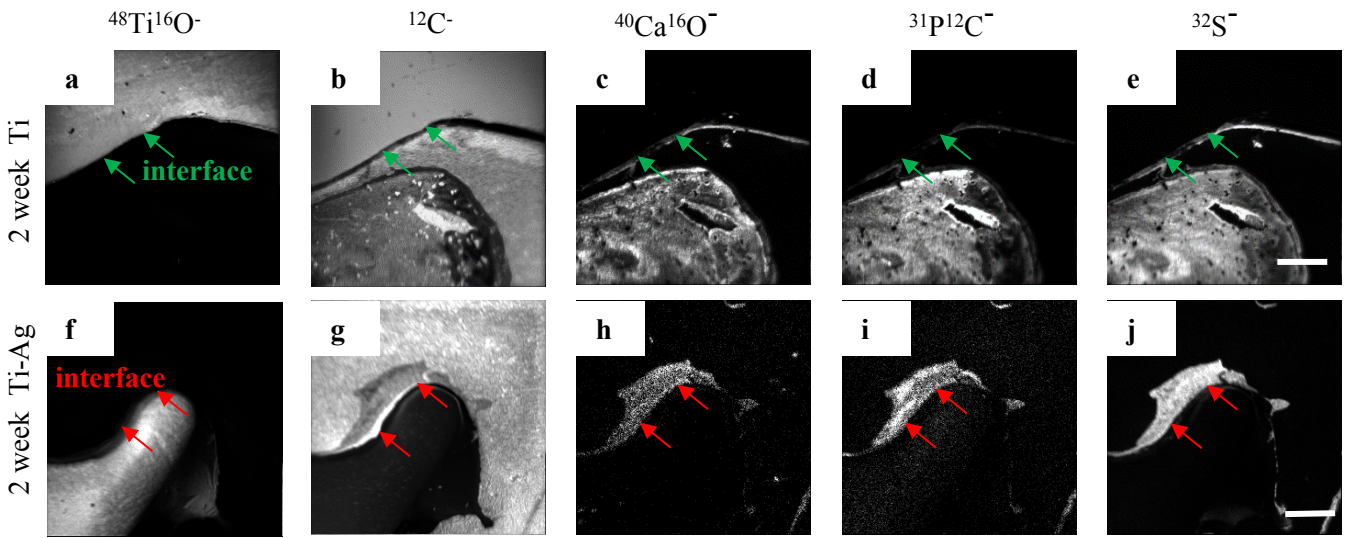


Fig. 6. NanoSIMS elemental images of bone-implant interface in (a-e) titanium and (f-j) silver coated titanium implants after 2 weeks implantation. The NanoSIMS images ($50 \times 50 \mu\text{m}^2$) were acquired using CAMECA NanoSIMS 50L instrument equipped with Cs^+ primary ion beam. Images reveal the colocalisation of sulfur (measured as $^{32}\text{S}^-$) and Ca/P (measured as $^{40}\text{Ca}^{16}\text{O}^-$ and $^{31}\text{P}^{12}\text{C}^-$, respectively). The arrows highlight the direct contact between the newly formed osseous tissue (measured as $^{40}\text{Ca}^{16}\text{O}^-$ and $^{31}\text{P}^{12}\text{C}^-$, respectively) and implants (measured as $^{48}\text{Ti}^{16}\text{O}^-$) in both groups. Scale bars $10 \mu\text{m}$.

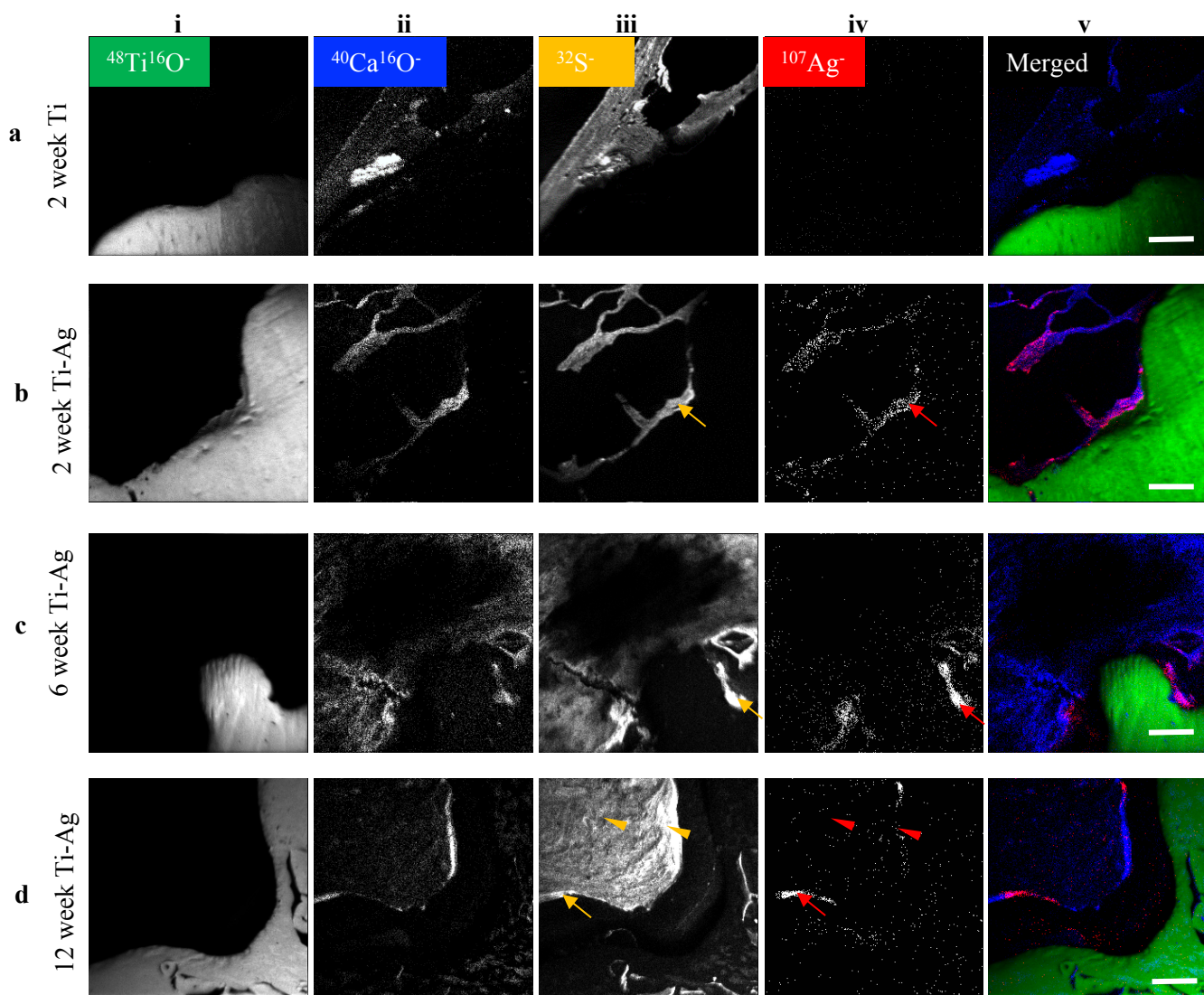


Fig. 7. NanoSIMS elemental images of bone-implant interface after (a-b) 2, (c) 6 and (d) 12 weeks implantation. The NanoSIMS images of $^{48}\text{Ti}^{16}\text{O}^-$ (i), $^{40}\text{Ca}^{16}\text{O}^-$ (ii), $^{107}\text{Ag}^-$ (iii), $^{32}\text{S}^-$ (iv) and merged (v) (superposition of $^{48}\text{Ti}^{16}\text{O}^-$, $^{40}\text{Ca}^{16}\text{O}^-$ and $^{107}\text{Ag}^-$) were used to determine the uptake of silver. A comparison of images in Ti and Ti-Ag group at 2 weeks post-implantation (a, b) reveals the silver (measured as $^{107}\text{Ag}^-$) is taken up into the osseous tissue (measured as $^{40}\text{Ca}^{16}\text{O}^-$). At 2 and 6 weeks post-implantation, the NanoSIMS images of $^{107}\text{Ag}^-$ (red arrows) and $^{32}\text{S}^-$ (yellow arrows) reveal the colocalisation of silver and sulfur in the newly formed bone. At 12 weeks post-implantation, colocalisation of $^{107}\text{Ag}^-$ (red arrow head) and $^{32}\text{S}^-$ (yellow arrow head) is only observed at the region near the periphery of implant. Scale bars 10 μm .

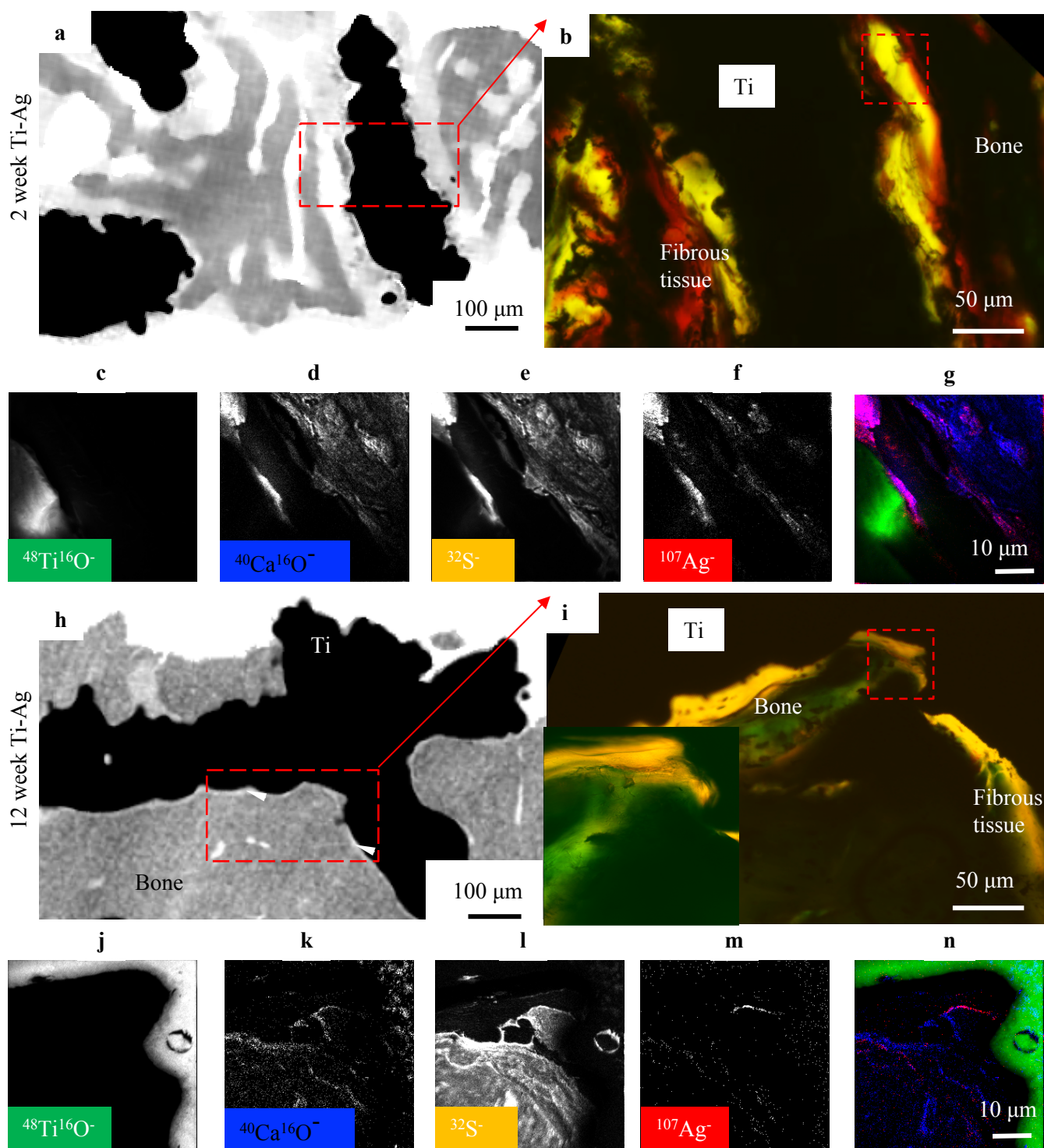


Fig. 8. (a-n) Correlative imaging of μCT , goldner's trichrome stained histology and NanoSIMS show different tissue types and the uptake of silver. At 2 weeks post-implantation, the newly formed bone is observed in both (a) μCT and (b) histology image. Correlative (b) histology and (c-g) NanoSIMS images shows the woven bone and fibrous tissue at the bone-implant interface. The colocalisation of silver and sulfur occurs in the newly formed woven bone. At 12 weeks post-implantation, the void space of the porous implant is filled with more matured bone, as shown in (h) μCT image. Correlative (i) histology and NanoSIMS images (j-n) show bone and fibrous tissue at the bone-implant interface.

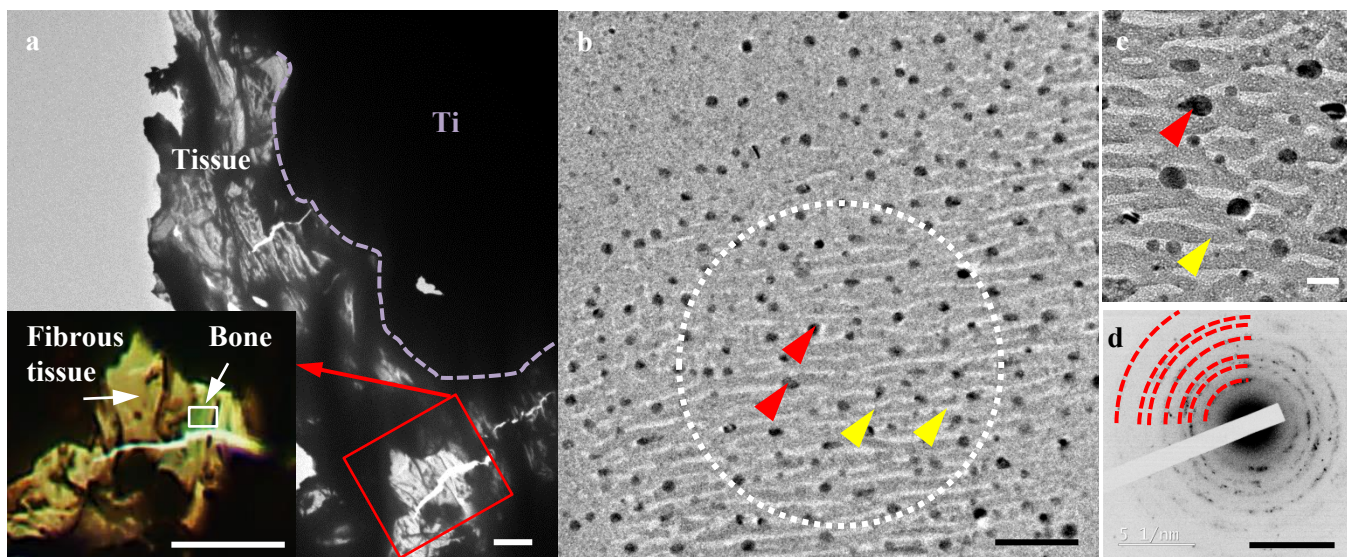


Fig. 9. (a) TEM image of a region containing a silver coated titanium scaffold and surrounding tissue at two weeks post implantation. The dotted line delineates the interface between titanium implant and regenerated tissue. Inset (from boxed area) is a histological image of an electron transparent tissue region adjacent to the implant that shows mineralised bone (stained green) next to fibrous connective tissue (stained orange). Higher magnification TEM images (b) & (c) from the area of bone identified in the inset (white box) reveals distinctive ~ 10 nm width fibrillar structures (yellow arrowheads) and electron dense particles (red arrowheads). The association of the fibrillary structures with the electron dense particles is conspicuous (c). A selected area electron diffraction (SAED) pattern of the encircled area in (b) was performed using a selected area aperture size of ~ 400 nm. The concentric rings (d) imply the presence of a crystalline nanoparticulate phase. The SAED pattern observed matches closely the standard silver sulfide pattern (dotted arc line in red) strongly supporting the hypothesis that the particles in the TEM images are silver sulfide. Scale bars = $10 \mu\text{m}$ in (a) and inset; (b) = 100 nm , (c) = 20 nm and (d) = 5 nm^{-1} (in reciprocal space).